

Quantum Simulation of the Dicke-Ising Model via Digital-Analog Algorithms

Dmitriy S. Shapiro^{1,*}, Yannik Weber², Tim Bode¹, Frank K. Wilhelm^{1,2}, and Dmitry Bagrets^{1,3}

¹*Peter Grünberg Institute, Quantum Computing Analytics (PGI-12),
Forschungszentrum Jülich, 52425 Jülich, Germany*

²*Theoretical Physics, Universität des Saarlandes, 66123 Saarbrücken, Germany and*

³*Institute for Theoretical Physics, University of Cologne, 50937 Köln, Germany*

The Dicke-Ising model, one of the few paradigmatic models of matter-light interaction, exhibits a superradiant quantum phase transition above a critical coupling strength. However, in natural optical systems, its experimental validation is hindered by a “no-go theorem”. Here, we propose a digital-analog quantum simulator for this model based on an ensemble of interacting qubits coupled to a single-mode photonic resonator. We analyze the system’s free energy landscape using field-theoretical methods and develop a digital-analog quantum algorithm that disentangles qubit and photon degrees of freedom through a parity-measurement protocol. This disentangling enables the emulation of a photonic Schrödinger cat state, which is a hallmark of the superradiant ground state in finite-size systems and can be unambiguously probed through the Wigner tomography of the resonator’s field.

I. INTRODUCTION

The Dicke-Ising model has garnered significant attention in recent years due to the richness of its quantum phases [1–8]. A central feature of this model is the competition between spin-spin interactions, which tend to drive an Ising transition, and the collective Dicke coupling, which leads to superradiant photon condensation. This interplay results in a more complex superradiant quantum phase transition (QPT) compared to that in the conventional Dicke model [9–15].

In natural optical systems, the superradiant QPT is generally considered forbidden by a no-go theorem, which asserts that the diamagnetic term—proportional to the square of the vector potential \mathbf{A}^2 —prevents photon condensation. However, this constraint can be circumvented [16–18] in quantum simulators such as cold atom lattices [19–26] or circuit QED setups [27–29] (see also review articles [30–32]), where the theorem is overcome on the physical level.

Another possibility to simulate the class of Dicke-like models could potentially be offered by quantum hardware, which relies on the Trotterized approximation of the evolution operator via quantum circuits. This approach, known as digital quantum simulation [33], has recently become a popular line of research and is considered one of the few promising future applications of quantum computers. Its validity has been successfully verified in numerous experiments, see recent reviews such as Ref. [34]. However, simulating many-body correlated systems with spin-boson or fermion-boson interactions presents a distinct challenge: encoding bosonic fields using qubits. Specifically, encoding a single bosonic mode with a finite occupation-number cutoff N_{\max} requires $\log_2 N_{\max}$ qubits [35, 36]. To address this problem, one may work within the alternative quantum digital-analog

framework [37–39]. The latter employs bosonic degrees of freedom as a computational resource and enables boson-qubit entanglement at the hardware level. Within this scheme, the dynamics of the quantum Rabi model in the strongly coupled limit was simulated using a single transmon qubit coupled to a resonator [38]. Our study leverages this methodology to simulate the dynamics governed by the more elaborate Dicke-Ising Hamiltonian, with a focus on novel qubit-boson architectures that are experimentally feasible within the context of circuit QED [38, 40].

A particularly compelling aspect of our digital-analog approach is twofold: (i) the potential to simulate the transition into the superradiant phase via a quench protocol, and (ii) the ability to disentangle the photon condensate and the qubit degrees of freedom in the many-body density matrix. This gives the proposed simulation strategy a striking advantage over fully analog simulators [23], where only macroscopic parameters of the condensate have been available for direct measurement. Remarkably, this disentanglement of condensed photons can enable the emulation of Schrödinger cat states, which are a hallmark of the superradiant ground state in finite-size systems.

The paper is organized as follows. In Section II, we present the model and the main idea of creating a cat-state density matrix with the help of qubit-parity measurements. In Section III, we provide a field-theory description of the superradiant QPT for different limits of the model. We introduce the method of deriving the free energy using path integrals in III A. The mean-field results for the conventional Dicke model and the Dicke-Ising model with spin-1/2 are discussed in III B and III C, respectively. The role of quantum fluctuations near the instanton trajectory and the relation to the Kibble-Zurek mechanism are addressed in III D. The generalization of the Dicke-Ising model to spins larger than 1/2, via angular bosonization, is provided in III E. A quasi-classical approach for angular fluctuations is presented in III F. In Section IV, we present the quantum simulation algo-

* d.shapiro@fz-juelich.de

rithm. We discuss the idea of the superradiant ground state approximation via the quench in IV A. In IV B, we present digital-analog quantum circuits for Jaynes-Cummings, Rabi and Dicke gates; in IV C we give an overview of the algorithm. In Section V, we discuss our results and present data for the exact and Trotterized dynamics; in the ending section VI we conclude.

II. MAIN IDEA

The Dicke-Ising model ($\hbar = k_B = 1$ hereafter),

$$\hat{H}_{\text{DI}} = \hat{H}_{\text{D}} - J \sum_{j=1}^{N-1} \hat{\sigma}_j^z \hat{\sigma}_{j+1}^z, \quad (1)$$

is a combination of the standard Ising model and the Dicke Hamiltonian

$$\hat{H}_{\text{D}} = \omega_0 \hat{a}^\dagger \hat{a} - \omega_z \sum_{j=1}^N \hat{\sigma}_j^z + \frac{g}{\sqrt{N}} (\hat{a}^\dagger + \hat{a}) \sum_{j=1}^N \hat{\sigma}_j^x, \quad (2)$$

which describes an ensemble of N spin- s degrees of freedom coupled to a common photon mode. In the Ising part of Eq. (1), a positive coupling $J > 0$ corresponds to a ferromagnetic spin-spin interaction. Through the Dicke part of Eq. (1), the spins obtain excitation frequencies $\omega_z > 0$, while the photon mode has frequency ω_0 and is described by the bosonic operators $[\hat{a}, \hat{a}^\dagger] = 1$; the qubit-resonator coupling strength is denoted by g . For qubits, which correspond to spin $s = 1/2$, we associate the logical $|0\rangle_j$ of qubit $j = 1, \dots, N$ to the eigenstate $(1, 0)^T$ of $\hat{\sigma}_j^z$ with the eigenvalue 1.

At zero temperature, g plays the role of a control parameter of the superradiant QPT. If g is less than the critical value, g_c , the system is in its normal phase, with a *ferromagnetic* ground state

$$|\text{FM}\rangle = |0\rangle \otimes \prod_{j=1}^N |0_j\rangle. \quad (3)$$

In the *superradiant* phase, where $g > g_c$, there exist two quasi-degenerate superradiant many-body states $|\Psi_R\rangle$ and $|\Psi_L\rangle$, and the highly entangled ground state becomes the superposition

$$|\text{SR}\rangle = \frac{1}{\sqrt{2}} (|\Psi_L\rangle + |\Psi_R\rangle) \quad (4)$$

In a large spin ensemble, these wave functions are given by the direct products $|\Psi_R\rangle = |-\alpha\rangle \otimes |R\rangle$ and $|\Psi_L\rangle = |\alpha\rangle \otimes |L\rangle$. Here, $|\pm\alpha\rangle = e^{-\frac{1}{2}|\alpha|^2} \sum_{n \geq 0} \frac{(\pm\alpha)^n}{\sqrt{n!}} |n\rangle$ are photon coherent states with opposite phases. The number of photons stored in these states, $|\alpha|^2$, can be macroscopically large. In the mean-field picture, the value of α is given by a free energy minimum. The qubit states

$|R(L)\rangle = \prod_{j=1}^N (|0\rangle_j \pm |1\rangle_j) / \sqrt{2}$ are anti-parallel to each other (on their respective single-particle Bloch spheres).

Let us remember that in circuit QED, Schrödinger's cat state is the nonclassical state

$$|\text{cat}\rangle = \frac{1}{\sqrt{2}} (|\alpha\rangle + |-\alpha\rangle), \quad (5)$$

which is a promising candidate for qubit encoding due to its non-locality in phase space [41–44], rendering it stable against local perturbations provided the photon number is large.

The central idea of our work is to disentangle $|\pm\alpha\rangle$ and $|R(L)\rangle$ from the joint many-body density matrix, $\hat{\rho}_{\text{SR}} = |\text{SR}\rangle\langle\text{SR}|$, thus emulating the cat state density matrix in the photon basis, i.e.,

$$\hat{\rho}_{\text{cat}} = \frac{1}{2} (|-\alpha\rangle\langle-\alpha| + |\alpha\rangle\langle\alpha| + |\alpha\rangle\langle-\alpha| + |-\alpha\rangle\langle\alpha|). \quad (6)$$

Note that simply taking the trace over the qubit degrees of freedom in $\hat{\rho}_{\text{SR}}$ results in a mixed-state density matrix

$$\hat{\rho}_{\text{mix}} = \text{tr}_\sigma[\hat{\rho}_{\text{SR}}] = \frac{1}{2} (|-\alpha\rangle\langle-\alpha| + |\alpha\rangle\langle\alpha|), \quad (7)$$

which lacks the coherent cross terms $|\pm\alpha\rangle\langle\mp\alpha|$ that appear in Eq. (6). To obtain these cross terms, we select one-half of the qubit states corresponding to a given value of the total qubit parity. This selective parity measurement can be defined as

$$\hat{\rho}_+ = \text{tr}_\sigma[\hat{\rho}_{\text{SR}} \hat{P}_+], \quad (8)$$

where the projection operator is

$$\hat{P}_+ = \frac{1}{2} \left(\hat{1} + \prod_{j=1}^N \hat{\sigma}_j^z \right), \quad (9)$$

with $\hat{P}_+|R\rangle = \hat{P}_+|L\rangle = (|R\rangle + |L\rangle) / \sqrt{2}$. The trace with the \hat{P}_+ in Eq. (8) provides the desired result, i.e. $\hat{\rho}_+ = \hat{\rho}_{\text{cat}}$. Performing a series of projective measurements following Eq. (8) enables us to observe nonclassical cat state signatures in a subsequent Wigner tomography [41, 42] of the photon mode.

Consider the Wigner function $W(x, p)$ corresponding to a reduced density matrix $\hat{\rho} = \text{tr}_\sigma[\hat{P} \hat{\rho}_{\text{SR}}]$,

$$W(x, p) = \sum_{n, m=0}^{\infty} \langle n | \hat{\rho} | m \rangle V_{n, m}(x, p), \quad (10)$$

where

$$V_{n, m}(x, p) = \int dy \frac{H_n(x-y) H_m(x+y) e^{2ipy - (x^2 + y^2)}}{\sqrt{\pi^{3/2} 2^{n+m} n! m!}} \quad (11)$$

are the harmonic oscillator eigenfunctions overlap integrals, and $H_n(x) = (-1)^n e^{x^2} d^n e^{-x^2} / dx^n$ are Hermite polynomials. Following to the definitions (7) and (8),

we have $\hat{\mathcal{P}} = \hat{1}$ for the mixed state and $\hat{\mathcal{P}} = \hat{P}_+$ for the cat state.

The momentum-integrated Wigner function yields the photon probability distribution $w(x) = \int dp W(x, p)$, which reduces to

$$w(x, t) = e^{-x^2} \sum_{n, m \geq 0} \frac{H_n(x) H_m(x)}{\sqrt{\pi 2^{n+m} n! m!}} \langle n | \hat{\rho}(t) | m \rangle. \quad (12)$$

In Fig. 1(a) and (b) we present, respectively, illustrations of the matrix elements of $\hat{\rho}_{\text{mix}}$ and $\hat{\rho}_+$ for a finite system in the superradiant phase. The many-body density matrix $\hat{\rho}_{\text{SR}}$ is found numerically via exact diagonalization of the Dicke-Ising Hamiltonian. One can observe that $\langle n | \hat{\rho} | m \rangle \neq 0$ if both of Fock state numbers n, m are odd. In the thermodynamic limit, $W_{\text{mix}}(x, p)$ would have two singular points at $x = \pm\sqrt{2}\alpha$; in a finite system near the critical point, $W_{\text{mix}}(x, p)$ has two linked blobs as shown in 1 (c).

The projected Wigner function $W_+(x, p)$ calculated from $\hat{\rho}_+$ is shown in Fig. 1(d). The signatures of Schrödinger's cat state are visible as fringes of negative quasi-probability, $W_+(x, p) < 0$, which is a benchmark for the presence of cat states in the output of our algorithm given below.

The remainder of the paper has two main threads: (i) Applying methods of statistical physics to derive a profile of the free energy. This sheds light on the order of

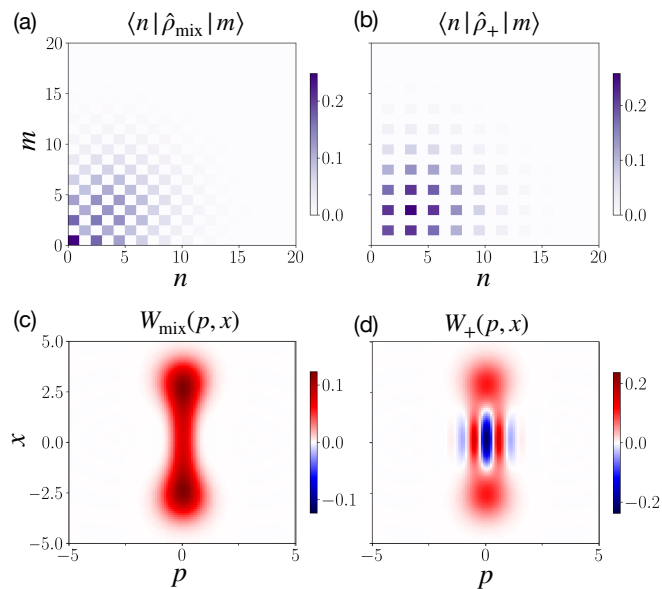


FIG. 1. Reduced density matrices (a) for the mixed state $\hat{\rho}_{\text{mix}} = \text{tr}_\sigma[\hat{\rho}_{\text{SR}}]$ and (b) when projected to the positive-parity subspace $\hat{\rho}_+ = \text{tr}_\sigma[\hat{\rho}_{\text{SR}}\hat{P}_+]$. (c) Wigner function of the mixed state, and (d) of the projected state showing non-classical features indicative of a cat state. The photon Hilbert space has a cutoff of 20 photons. The coupling $g = 0.9\sqrt{\omega_0 J}$ is near the critical value \tilde{g}_c , the chain has open ends and comprises $N = 7$ qubits. The other parameters are $J = \omega_0$ and $\omega_z = 0.05\omega_0$.

the QPT as well as on the quantum fluctuations around the mean-field solutions and the associated macroscopic quantum tunneling between the superradiant states $|\Psi_L\rangle$ and $|\Psi_R\rangle$. (ii) Based on this understanding of the free energy profile, we then perform quantum-circuit simulations of the real-time dynamics of the photon distribution in the corresponding effective potential, culminating in the sought-for cat states.

III. SUPERRADIANT QUANTUM PHASE TRANSITIONS

In this section, we start with a recapitulation of the well-known result about the second-order QPT in the conventional Dicke model. After that, we turn to the Dicke-Ising Hamiltonian Eq. (1) with $J \neq 0$ and $\omega_z = 0$; the limit $\omega_z \rightarrow 0$ enables an exact calculation of the trace over the spins. It can be performed for qubits ($s = 1/2$) via the usual Jordan-Wigner transformation, resulting in a mean-field solution for the free energy that predicts a first-order QPT. Besides that, the free energy determines an instanton trajectory in Matsubara imaginary time and, therefore, the rate of macroscopic quantum tunneling.

For $\omega_z \ll J$, in the superradiant phase, the order-parameter fluctuations are critical because the magnon excitations become gapless (Eq. (22)). If the fluctuations are unstable, the Gaussian approximation is not sufficient. If s is large (qudit case), and the photon mode has a low frequency, then fluctuations are suppressed; the mean-field solution becomes asymptotically exact in this case. At finite $\omega_z \sim J$, integrating out the magnons exactly via the Jordan-Wigner transformation is more challenging. As an alternative approach, we therefore suggest the angular representation of spins, which is valid for arbitrary s .

A. Methods

To calculate the free energy F as a function of the superradiant order parameter, we recall the relation between F and the partition function $Z = \text{tr} e^{-\hat{H}/T}$ at finite temperature T ,

$$Z = e^{-F/T}, \quad (13)$$

where the trace is taken over all degrees of freedom. Field-theory methods enable one to represent the trace as a path integral over complex bosonic fields, a and \bar{a} , while the fields $\vec{\sigma}$ parameterize the spin sector, i.e. the partition function may be written as

$$Z = \int d[a, \bar{a}, \vec{\sigma}] e^{-S[a, \bar{a}, \vec{\sigma}]}. \quad (14)$$

Upon transformation from a Hamiltonian to the path integral, the real part of the photon operators becomes

a trajectory $u(\tau)$ on the Matsubara time interval $\tau \in [0, 1/T]$,

$$\frac{1}{\sqrt{N}}(\hat{a} + \hat{a}^\dagger) \rightarrow u(\tau). \quad (15)$$

The trajectories $u(\tau)$ are slow if N is large (thermodynamic limit) and the photon frequency ω_0 is small. This corresponds to the mean-field limit, where u can be associated with the superradiant order parameter. The photon position operator, $\hat{x} = \frac{1}{\sqrt{2}}(\hat{a} + \hat{a}^\dagger)$, is related to u by $\hat{x} \rightarrow \sqrt{N/2}u$.

The idea now is to calculate the path integral over all *fast* fields and represent the partition function as a single path integral over the *slow* quantum field u , i.e. $Z = \int D[u] \exp(-S_{\text{eff}}[u])$; the new functional in the exponential is the effective action for u . The free energy follows from S_{eff} if we neglect the slow time dependence of $u(\tau)$ to obtain

$$F(u) = TS_{\text{eff}}[u = \text{const.}]. \quad (16)$$

The low-temperature action S_{eff} is proportional to $1/T$; hence, T drops from all the formulas for the free energy.

Note that the momentum operator $\hat{p} = \frac{i}{\sqrt{2}}(\hat{a} - \hat{a}^\dagger)$ does not appear in the interacting part of the Hamiltonian (1). Therefore, in the path integral, the real field v corresponding to $i\hat{p}$ appears only in the free photon Matsubara action, namely

$$S_0 = \int_0^{1/T} d\tau \bar{a}(\partial_\tau + \omega_0)a, \quad (17)$$

where $a(\tau)$ and $\bar{a}(\tau)$ are complex bosonic fields. If we make a rotation to the real fields, $u = (a + \bar{a})/\sqrt{N}$ and $v = i(a - \bar{a})/\sqrt{N}$, and integrate out the field v , we arrive at the free action for the order parameter,

$$S_0[u] = N \int_0^{1/T} d\tau \mathcal{L}[u(\tau)], \quad (18)$$

with the Lagrangian

$$\mathcal{L} = \frac{(\partial_\tau u)^2}{4\omega_0} + \frac{\omega_0}{4}u^2. \quad (19)$$

This is the sum of the kinetic term $\sim (\partial_\tau u)^2$ and the potential energy $\mathcal{F}_0 = \omega_0 u^2/4$, which determines the parabolic free energy profile. In the next Section, we show how the interaction with the spins contributes additional terms to \mathcal{F} .

B. Free energy in the Dicke model

Consider the conventional Dicke Hamiltonian (2). In what follows, we work with the normalized free energy,

$\mathcal{F} = F/N$, which, in the thermodynamic limit, reads

$$\mathcal{F}_D(u) = \frac{\omega_0}{4}u^2 - \omega_z \left(\sqrt{1 + \frac{g^2}{\omega_z^2}u^2} - 1 \right). \quad (20)$$

This result has been derived by integrating out the qubit states, which can be done via different spin representations such as Holstein-Primakoff bosonization [10] or bilinear combinations of fermion fields [9, 11, 15]. The Dicke free energy $\mathcal{F}_D(u)$ possesses a second-order QPT, as shown in Fig. 2 (a-c). In the normal phase $g < g_c = \sqrt{\omega_0\omega_z/2}$ below the critical coupling, there is only one minimum at $u = 0$. At $g = g_c$, the QPT occurs. Finally, there is a superradiant phase at $g > g_c$, which means that $\mathcal{F}_D(u)$ acquires two minima at $u = \pm u_0$, $u_0 > 0$, and the system spontaneously relaxes to one of them.

C. Free energy in the Dicke-Ising model at $\omega_z = 0$ and $s = 1/2$

Coming back to the Dicke-Ising Hamiltonian with $J > 0$, we consider the limit of $\omega_z \rightarrow 0$. In Appendix A, we apply the Jordan-Wigner transformation for spin operators and perform the subsequent integral over the fermion fields. As a result, we obtain the mean-field free energy

$$\mathcal{F}_{DI}(u) = \frac{\omega_0}{4}u^2 - \frac{2}{\pi}(g|u| + J)\text{E} \left(\frac{4g|u|J}{(g|u| + J)^2} \right), \quad (21)$$

where the elliptic function $\text{E}(x)$ results from an integral over the quasi-momentum in the Brillouin zone $\mathbf{k} \in (-\pi, \pi)$. One obtains two bands of Ising-chain magnons in the Brillouin zone, and their spectrum is

$$\epsilon(\mathbf{k}) = \pm 2\sqrt{g^2u^2(\tau) + J^2 - 2Jgu \cos \mathbf{k}}. \quad (22)$$

In contrast to \mathcal{F}_D , the function \mathcal{F}_{DI} has three minima in a certain range of g around the critical $\tilde{g}_c = c_0\sqrt{\omega_0 J}$, $c_0 \approx 0.9$. The first-order QPT occurs when the two side minima become lower than the central minimum at $u = 0$ (see Fig. 2(d-f)). Note that our approach is complementary to previous studies of phase transitions in this model [1–8].

D. Instanton approach. Relation to Ising transition and Kibble-Zurek mechanism

The free energy \mathcal{F}_{DI} given by (21) is part of a mean-field Matsubara action where $u(\tau)$ is a trajectory in imaginary time,

$$S_{\text{mf}} = N \int_0^{1/T} d\tau \left(\frac{(\partial_\tau u)^2}{4\omega_0} + \mathcal{F}_{DI}(u) \right). \quad (23)$$

Variation of this action yields an instanton equation that describes macroscopic quantum tunneling between the

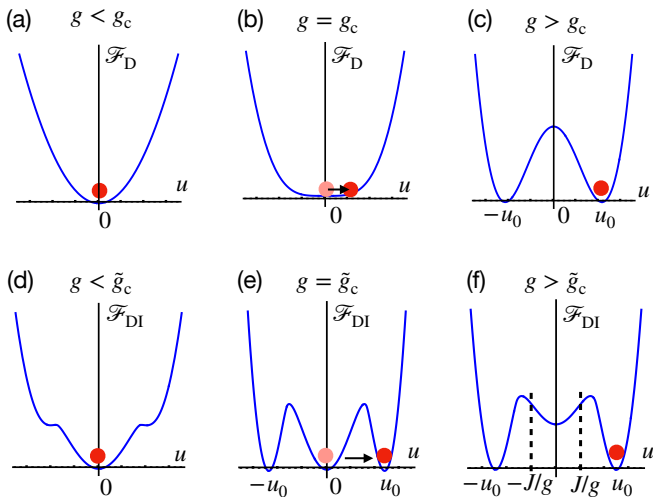


FIG. 2. Sketch of the free energies as functions of the superradiant order parameter for (a-c) the Dicke and (d-f) the Dicke-Ising model. (a, d) Normal phases. Critical points (b) of the second-order and (e) first-order QPTs. (d, f) Superradiant phases. The values $u = \pm J/g$ in (f) correspond to the critical Ising chain.

minima of the free energy at $u = \pm u_0$, see Appendix B. The solution of the instanton trajectory, $u_{\text{inst}}(\tau)$, can be defined implicitly via

$$\tau = \int_{-u_0}^{u_{\text{inst}}(\tau)} \frac{du}{\sqrt{2\omega_0(\mathcal{F}_{\text{DI}}(u) - \mathcal{F}_{\text{DI}}(-u_0))}}. \quad (24)$$

We find that in the superradiant phase, the instanton trajectory always crosses two special points $u = \pm J/g$, see Fig. 2(f). According to Eq. (22) for the magnon spectrum, the Ising chain becomes critical due to the gap closing at these points. This crossing occurs because u_{inst} has support in the interval $[-u_0; u_0]$, which includes these special points since $|J/g| < u_0$, as implied by Eq. (21). We conclude that the fluctuations above the QPT are non-vanishing; in other words, the system remains critical in the superradiant phase. This behavior contrasts with the conventional Dicke model, which is critical only at the transition point. We can also draw an imaginary-time analogy of the Kibble-Zurek mechanism around the second-order Ising QPT. In our case, the Ising transition is virtual and hidden in the superradiant phase.

E. Angular representation at $\omega_z \neq 0$ and $s > 1/2$

As mentioned above, the presence of special points on the instanton trajectory indicates critical fluctuations at $\omega_z = 0$ in this model, attributed to the gapless spectrum. However, the gap re-emerges at finite ω_z . The analytic derivation of \mathcal{F}_{DI} for this general case of $\omega_z \neq 0$ is more involved: Neither the Jordan-Wigner nor the Majorana representation of the Pauli operators yields a quadratic

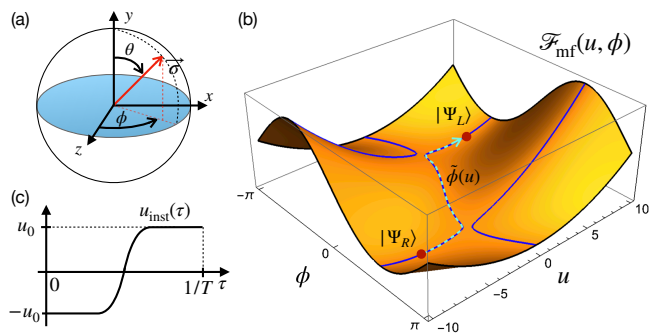


FIG. 3. (a) Angular representation of qubit states. The xz -plane contributing most to the mean-field solution is shown in blue. (b) The effective potential in the mean-field approximation. The red dots are the two minima representing the superradiant states $|\Psi_{R,L}\rangle$. The dashed curve is an instanton trajectory. (c) Schematic representation of the instanton trajectory $u_{\text{inst}}(\tau)$.

action over fermions. Therefore, the exact Gaussian integration over spin states used in the derivations of Eq. (20) and (21), does not apply.

An alternative representation of spins with arbitrary s is provided by (sketch shown in Fig. 3(a))

$$\begin{aligned} \hat{\sigma}_j^x &\rightarrow 2s \sin \theta_j \sin \phi_j, \\ \hat{\sigma}_j^y &\rightarrow 2s \cos \theta_j, \\ \hat{\sigma}_j^z &\rightarrow 2s \sin \theta_j \cos \phi_j. \end{aligned} \quad (25)$$

As the number of excited states is $2s$, qubits correspond to $s = 1/2$, *qutrits* to $s = 1$, and so on. In the path integral for the partition function, θ_j and ϕ_j are real bosonic fields,

$$Z = \int d[\{\phi, \theta\}_j^N, u] \exp(-S[\{\phi, \theta\}_j^N, u]), \quad (26)$$

and the full Matsubara action reads

$$S = S_{\text{WZNW}} + \int_0^{1/T} d\tau (\bar{a} \partial_\tau a + H_{\text{DI}}). \quad (27)$$

This is the sum of the Wess-Zumino-Novikov-Witten action

$$S_{\text{WZNW}} = -is \sum_j \int_0^{1/T} d\tau \dot{\phi}_j (1 - \cos \theta_j), \quad (28)$$

i.e. the integral over the spin Berry phase, the kinetic term for the photon field $\sim \bar{a} \partial_\tau a$, and finally the Dicke-Ising Hamiltonian parameterized by Eq. (25).

In the limit of small photon frequency, $\omega_0 \ll J$, g and finite ω_z , a mean-field solution can be found as this regime of energy scales allows one to consider $u(\tau)$ as a *slow* variable. The trajectories contributing to Z then effectively

reside near the xz -plane, with small, rapid out-of-plane fluctuations, i.e.

$$\theta_j(\tau) = \frac{\pi}{2} + \Delta\theta_j(\tau). \quad (29)$$

The corresponding geometric interpretation is shown in Fig. 3(a). The logic of separation into slow and fast components is also applicable to the in-plane components

$$\phi_j(\tau) = \phi(\tau) + \Delta\phi_j(\tau), \quad (30)$$

with a slow collective angle $\phi(\tau)$ and rapid fluctuations $\Delta\phi_j(\tau)$.

F. Quasi-classical approach for fluctuations

Further progress can be achieved in the quasi-classical limit where one assumes that the fluctuations near the mean-field trajectory are small. We start from the mean-field solution for free energy, neglecting all angle fluctuations, i.e. $\Delta\theta_j(\tau) = \Delta\phi_j(\tau) = 0$. We also assume that ω_0 is smaller than other energy scales, which guarantees that $u(\tau)$ and $\phi(\tau)$ are slow. The resulting mean-field action reads

$$S_{\text{mf}} = N \int_0^\infty d\tau \left(\frac{(\partial_\tau u)^2}{4\omega_0} + \mathcal{F}_{\text{mf}}(u, \phi) \right), \quad (31)$$

where the mean-field free energy is

$$\mathcal{F}_{\text{mf}}(u, \phi) = \frac{1}{4}\omega_0 u^2 + h(u, \phi). \quad (32)$$

Here, $h(u, \phi)$ corresponds to the spin part of the Hamiltonian with homogeneous configurations of $\phi_j = \phi$ and $\theta_j = \pi/2$,

$$h(u, \phi) = 2s(-\omega_z \cos \phi + gu \sin \phi - 2sJ \cos^2 \phi). \quad (33)$$

The profile of (33) in the superradiant phase is shown in Fig. 3(b), where the two minima correspond to the distinct macroscopic superradiant states $|\Psi_R\rangle$ and $|\Psi_L\rangle$. As long as there is no time-derivative term for ϕ in S_{mf} , non-trivial contributions to Z are given only by the single quantum trajectory $\tilde{\phi}(u_{\text{inst}})$ that connects these two minima, i.e.

$$Z \sim e^{-S_{\text{mf}}[u_{\text{inst}}(\tau)]}. \quad (34)$$

The value of Z then determines the amplitude of macroscopic quantum tunneling.

The angular dependence $\tilde{\phi}(u)$ is determined by the condition $\partial_\phi \mathcal{F}_{\text{mf}}(u, \phi) = 0$. The motion of $u(\tau)$ along the quantum trajectory is described by a modified instanton equation

$$\frac{\ddot{u}}{2\omega_0} + \partial_u \mathcal{F}_{\text{mf}}(u, \tilde{\phi}(u)) = 0 \quad (35)$$

with boundary conditions $u(0) = -u(1/T) = -u_0$. Again, a sketch of the instanton solution is shown in Fig. 3(c).

The next step of our quasi-classical approach is to calculate the quantum corrections \mathcal{F}_fl to the mean-field potential \mathcal{F}_{mf} caused by the Gaussian fluctuations of $\Delta\theta_j(\tau)$ and $\Delta\phi_j(\tau)$ neglected previously. To this end, we expand S given by (27) to second order in $\Delta\theta_j(\tau)$ and $\Delta\phi_j(\tau)$,

$$S = S_{\text{mf}}[u, \phi] + S_{\text{G}}[u, \phi, \Delta\theta, \Delta\phi]. \quad (36)$$

This is a sum of the mean-field action (33) and the Gaussian part S_{G} given by

$$S_{\text{G}} = \frac{1}{2} \int_0^{1/T} d\tau \int_{-\pi}^{\pi} \frac{d\mathbf{k}}{2\pi} [\Delta\theta \ \Delta\phi]_{-\mathbf{k}} \begin{bmatrix} \mathcal{A}(u, \phi) & -is\partial_\tau \\ is\partial_\tau & \mathcal{B}_{\mathbf{k}}(u, \phi) \end{bmatrix} \begin{bmatrix} \Delta\theta \\ \Delta\phi \end{bmatrix}_{\mathbf{k}}, \quad (37)$$

where the matrix elements depend on the slow trajectories. Note that the action does not have a linear contribution because we assume that $\sum_j \Delta\theta_j = \sum_j \Delta\phi_j = 0$. For the term $\sim \Delta\theta^2$, the element \mathcal{A} partially coincides with h from (32),

$$\mathcal{A}(u, \phi) = 4Js^2 \cos^2 \phi - h(u, \phi). \quad (38)$$

The amplitude of the term $\sim \Delta\phi^2$ involves the momentum dependence

$$\mathcal{B}_{\mathbf{k}}(u, \phi) = \mathcal{A}(u, \phi) - 8Js^2 \sin^2 \phi \cos \mathbf{k}. \quad (39)$$

The stability of the action (37) along the trajectory $\tilde{\phi}(u)$ is provided by the joint condition $\mathcal{A}(u, \phi) > 0$ and $\mathcal{B}_{\mathbf{k}}(u, \phi) > 0$ for all \mathbf{k} . It is equivalent to

$$4sJ \cos 2\phi + \omega_z \cos \phi - gu \sin \phi > 0. \quad (40)$$

Assuming that (40) is satisfied and u and ϕ are slow (adiabatic limit), the Gaussian integration over the fields $\Delta\theta_{\mathbf{k}}$ and $\Delta\phi_{\mathbf{k}}$ yields the fluctuation correction $S_{\text{fl}}[u, \phi]$ to the mean-field action. This correction reads

$$S_{\text{fl}} = N \int_{-\pi}^{\pi} \frac{d\mathbf{k}}{2\pi} \ln \prod_{n \geq 1} \left(1 + \frac{\mathcal{A}(u, \phi) \mathcal{B}_{\mathbf{k}}(u, \phi)}{(2\pi s T n)^2} \right). \quad (41)$$

We calculate the infinite product over the Matsubara index $n \geq 1$ using the identity (A12) from the Appendix. After that, we take the limit $T \rightarrow 0$ in the definition for the free energy correction $\mathcal{F}_{\text{fl}} = N^{-1} T S_{\text{fl}}$ and find

$$\mathcal{F}_{\text{fl}}(u, \phi) = \frac{1}{2s} \int_{-\pi}^{\pi} \frac{d\mathbf{k}}{2\pi} \sqrt{\mathcal{A}(u, \phi) \mathcal{B}_{\mathbf{k}}(u, \phi)}. \quad (42)$$

The integral over \mathbf{k} yields

$$\mathcal{F}_{\text{fl}}(u, \phi) = \frac{1}{\pi s} \sqrt{\mathcal{A}(u, \phi) (\mathcal{A}(u, \phi) + 8s^2 J \sin^2 \phi)} \times \text{E} \left(\frac{16s^2 J \sin^2 \phi}{\mathcal{A}(u, \phi) + 8s^2 J \sin^2 \phi} \right). \quad (43)$$

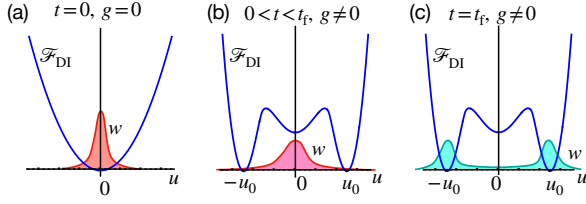


FIG. 4. Sketch illustrating the quench dynamics of the photon probability distribution $w(x, t)$ in the potential formed by the free energy $\mathcal{F}_{\text{DI}}(u)$. (a) Gaussian $w(x, t)$ at $t = 0$ when $g = 0$. (b) Evolution of $w(x, t)$ after the quench of g from 0 to $g \approx g_c$. (c) End of the evolution at $t = t_f$ shows two maxima of $w(x, t_f)$ at $u = \pm u_0$ corresponding to superradiant condensates.

In the Dicke-model limit, $J = 0$, we use $\mathcal{A} = -h$ and obtain

$$\mathcal{F}_{\text{fl}} = -\frac{1}{2s}h(u, \phi). \quad (44)$$

The full free energy then reads

$$\mathcal{F}_{\text{mf}} + \mathcal{F}_{\text{fl}} = \frac{1}{4}\omega_0 u^2 + \left(1 - \frac{1}{2s}\right)h(u, \phi). \quad (45)$$

One can see from (45) that the fluctuation correction is small at $s \gg 1$. The Dicke model for large spins has been studied recently in Ref. [45] where the authors predicted multicritical behavior at QPT. For nonzero J , one also finds $\mathcal{F}_{\text{fl}}/\mathcal{F}_{\text{mf}} \sim s^{-1}$. Therefore, in the large-spin limit, the fluctuations are small and the quasi-classical approach is legitimate.

In the following, based on our understanding of the free energy profile \mathcal{F} , we formulate a quench protocol for the simulation of the condensate dynamics.

IV. HYBRID QUANTUM CIRCUIT

A. Approximation of the superradiant ground state via quench

Our remaining objective is to obtain an approximate superradiant state from a finite quantum circuit, which takes the form of unitary evolution on the time interval $t \in [0; t_f]$ starting from the trivial ferromagnetic state for spin $s = 1/2$, $|\Psi_0\rangle = |\text{FM}\rangle$. Note that $|\text{FM}\rangle$ is an eigenstate of \hat{H}_{DI} at $g = 0$. The final state $|\Psi_t\rangle = e^{-i\hat{H}_{\text{DI}}t}|\Psi_0\rangle$ is supposed to be close to the exact eigenstate $|\text{SR}\rangle$. The evolution with \hat{H}_{DI} can be understood as a quench after the coupling g is switched on at $t = 0$.

In coordinate representation, the photon distribution at $t = 0$ is a Gaussian wave packet, i.e.

$$w(u, t=0) = \frac{1}{\sqrt{\pi}}e^{-u^2N}, \quad (46)$$

which can be interpreted as an eigenstate of a particle in the parabolic free energy profile $\mathcal{F}_{\text{DI}}(u)$ at $g = 0$, see

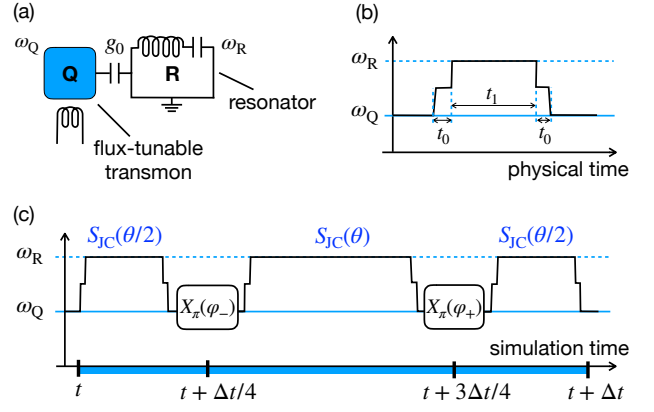


FIG. 5. (a) Qubit-resonator architecture for the Rabi model. (b) Resonant pulse for the Jaynes-Cummings gate. (c) Pulse sequence representing the Rabi gate.

Fig. 4(a). We note that, when sending $N \rightarrow \infty$, the wave packet $w(u, t)$ tends to a δ -singularity, which is the classical limit.

As sketched in Fig. 4(b), the quench induces an instantaneous change to $\mathcal{F}_{\text{DI}}(u)$, and the Gaussian packet tunnels into the side minima; the evolution should stop at the moment $t = t_f$ when $w(u, t_f)$ is concentrated in either of these minima (Fig. 4(c)). The many-body wave function $|\Psi_t\rangle$ then contains a substantial amount of condensed photons, which is used in the further protocol detailed below.

B. Rabi, Jaynes-Cummings, and Dicke gates

We take inspiration from the digital-analog approach of Ref. [37, 38], where the authors suggested to simulate the quantum Rabi model

$$\hat{H}_{\text{R}} = \omega_0 \hat{a}^\dagger \hat{a} + g(\hat{a} + \hat{a}^\dagger)\hat{\sigma}^x \quad (47)$$

through a combination of single-qubit rotations and a hybrid Jaynes-Cummings (JC) gate

$$\hat{S}_{\text{JC}}(\theta) = \exp(-i\theta(\hat{a}^\dagger \hat{\sigma}^- + \hat{a} \hat{\sigma}^+)), \quad (48)$$

where $\hat{\sigma}^\pm = \frac{1}{2}(\hat{\sigma}^x \mp i\hat{\sigma}^y)$. The JC gate enables efficient rotations in the joint qubit-resonator Hilbert space. We have in mind an architecture as shown in Fig. 5(a), where a tunable transmon qubit (Q) with physical frequency ω_{Q} is coupled to a superconducting resonator (R), modeled as an LC -circuit with fundamental frequency ω_{R} . The JC gate can be implemented as a flux pulse applied to Q, similar to two-qubit XY -gates [46]. A sketch of the pulse envelope is shown in Fig. 5(b). The pulse tunes ω_{Q} into a resonance with ω_{R} during the *physical* time t_1 , which enables the system to acquire the desired relative phase $\theta = g\Delta t = g_0 t_1$ where Δt is the Trotterization time *in the simulation*, and g_0 is the *physical* qubit-resonator coupling. The additional buffer steps t_0 may be used to gauge out dynamic phases in \hat{S}_{JC} .

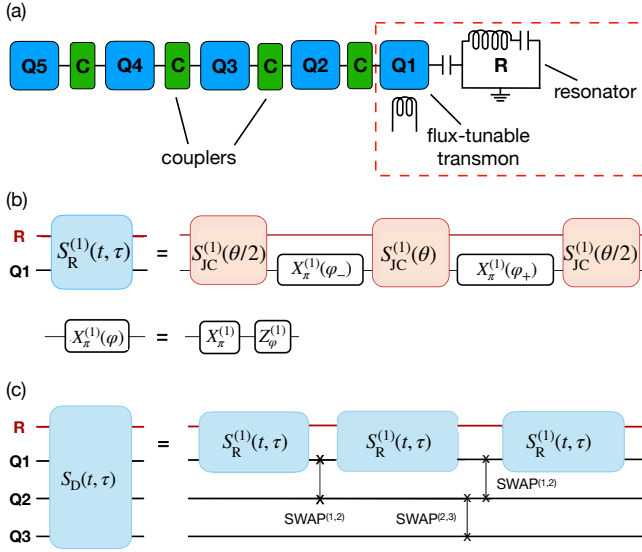


FIG. 6. (a) Qubit-boson architecture for the Dicke-Ising model. Dashed red box: Rabi gate block for the first qubit. Also shown are quantum circuits representing (b) the Rabi and (c) Dicke gates. The gate $X_\pi^{(1)}(\varphi)$ is acting to the first qubit.

Reproducing the logic of Ref. [38], we now derive the Rabi gate from the JC gate and then generalize the former to a Dicke gate. The original idea is to decompose Eq. (47) into

$$\hat{H}_R = \frac{1}{2}(\hat{H}_{JC} + \hat{H}_{AJC}) \quad (49)$$

where

$$\hat{H}_{JC} = \hat{H}_0 + 2g(\hat{a}^\dagger \hat{\sigma}^- + \hat{a} \hat{\sigma}^+) \quad (50)$$

is the Jaynes-Cummings Hamiltonian and

$$\hat{H}_{AJC} = \hat{\sigma}^x \hat{H}_{JC} \hat{\sigma}^x \quad (51)$$

is the corresponding counter-rotating interaction term. The free part can be chosen as

$$\hat{H}_0 = \omega_0(\hat{a}^\dagger \hat{a} - \hat{\sigma}^z/2). \quad (52)$$

The exact Trotter step $e^{-i\hat{H}_R \Delta t}$ on the simulation time interval $[t; t + \Delta t]$ is approximated to second order by

$$\hat{U}_R(t + \Delta t, t) = e^{-i\hat{H}_{JC} \Delta t/4} e^{-i\hat{H}_{AJC} \Delta t/2} e^{-i\hat{H}_{JC} \Delta t/4}, \quad (53)$$

which has a discretization error of $\mathcal{O}(\Delta t^3)$. Moving to the frame rotating with \hat{H}_0 , one obtains

$$\hat{U}_R(t + \Delta t, t) = e^{-i\hat{H}_0(t+\Delta t)} \hat{S}_R(t + \Delta t, t) e^{i\hat{H}_0 t} \quad (54)$$

where \hat{S}_R is the hybrid qubit-resonator gate sequence

$$\hat{S}_R = \hat{S}_{JC}(\theta/2) \hat{X}_\pi(\varphi_+) \hat{S}_{JC}(\theta) \hat{X}_\pi(\varphi_-) \hat{S}_{JC}(\theta/2). \quad (55)$$

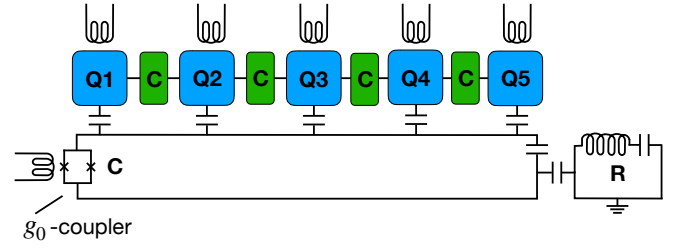


FIG. 7. Alternative qubit-boson architecture with all qubits tunable and coupled to the resonator. The auxiliary qubit acts as a coupler (C) to the resonator with tunable g_0 .

where the phases are $\varphi_- = \omega_0(t + \Delta t/4)$ and $\varphi_+ = \omega_0(t + 3\Delta t/4)$. This gate has been realized experimentally as a pulse sequence [38], which is shown schematically in Fig. 5(c). It consists of three analog JC gates separated by single-qubit gates, which we have combined in the definition

$$\hat{X}_\pi(\varphi_\pm) = \exp(-i\varphi_\pm \hat{\sigma}^z) \hat{\sigma}^x. \quad (56)$$

These single-qubit gates encode the counter-rotating evolution due to \hat{H}_{AJC} as well as the necessary rotating-frame transformations.

With the multi-qubit architecture of Fig. 6(a) in mind, where only one qubit is *physically* coupled to the resonator, we propose a Dicke gate \hat{S}_D implemented by applying the Rabi gate Fig. 6(b) to Q1 only, while digital SWAP gates mediate the interaction to the other qubits Q2 and Q3 (Fig. 6(c)). An alternative architecture analogous to the experimental setting of Ref. [40] is suggested in Fig. 7. Compared to Fig. 6(a), all qubits are tunable and directly coupled to the resonator via the additional g_0 -coupler. Rabi gates can then be applied to each of the qubits without the need for additional SWAP gates.

C. Algorithm overview

The full algorithm, which starts from $|\Psi_0\rangle$, is shown in Fig. 8. In each Trotter step, the Dicke gate \hat{S}_D is followed by a set of single-qubit Z -gates and two-qubit ZZ -gates, which simulate the on-site frequencies ω_z and the Ising interactions in Eq. (1) via

$$ZZ_{\eta,j} = e^{i\eta \hat{\sigma}_j^z \hat{\sigma}_{j+1}^z}, \quad Z_{\beta,j} = e^{i\beta \hat{\sigma}_j^z}, \quad (57)$$

where the phases are given by $\eta = J\Delta t$ and $\beta = \omega_z \Delta t$. Together, these gates constitute our Dicke-Ising gate \hat{S}_{DI} . At the end of the full Trotter evolution, we arrive at the many-body state $|\Psi_{t_f}\rangle \approx |\text{SR}\rangle$ that approximates the exact superradiant state. The Trotter evolution is followed by a CNOT sequence (emulating \hat{P}_+) and measurement of the first qubit. As proposed in [47], this CNOT sequence yields the parity by measuring only a single qubit instead of all of them. If the measurement result is $z_1 = 1$, then one performs Wigner tomography

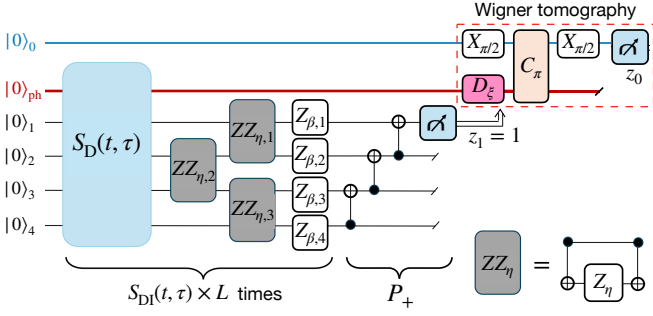


FIG. 8. Full quantum circuit implementing the cat state and Wigner tomography. The circuit with L Trotter steps and N qubits requires $3LN$ JC gates and $(2L+1)(N-1)$ two-qubit CNOT-gates. Assuming the architecture shown in Fig. 6(a), the algorithm involves $\frac{1}{2}LN(N-1)$ SWAPs. The alternative architecture from Fig. 7 does not require SWAPs.

of the resonator. If $z_1 = -1$, the tomography is not performed. This completes our algorithm.

The Wigner tomography circuit is shown in Fig. 8 inside the dashed contour. We follow the ideas of the measurement protocols suggested in Refs. [38, 42, 48]. There is a representation of the Wigner function equivalent to Eq. (10) that reads

$$W_\xi = \frac{2}{\pi} \text{tr}(\hat{\Pi} \hat{D}_\xi^\dagger \hat{\rho}_{\text{ph}} \hat{D}_\xi), \quad (58)$$

where the photon-state density matrix ρ_{ph} is given by the projection of the full many-body state on a certain spin configuration. Here, $\hat{\Pi} = e^{i\pi \hat{a}^\dagger \hat{a}}$ is the photon parity operator, $\hat{D}_\xi = e^{\xi \hat{a}^\dagger - \xi^* \hat{a}}$ is the standard displacement operator with the complex phase $\xi = x + ip$ parameterized by x and p . The displacement operator can be implemented as a drive pulse applied to the resonator. It is depicted as the gate D_ξ in Fig. 8. The density matrix $\hat{\rho}_{\text{ph}}$ becomes $\hat{D}_\xi^\dagger \hat{\rho}_{\text{ph}} \hat{D}_\xi$ after this pulse. The parity operator $\hat{\Pi}$ is implemented (i) via the gate C_π entangling the resonator with an off-resonant ancilla qubit and (ii) via two $X_{\pi/2}$ gates to perform Ramsey interferometry. Measuring the ancilla in the computational basis yields the photon parity $\Pi = \pm 1$ via the measurement value z_0 . The measurement is performed repeatedly to obtain the respective probabilities $\mathcal{P}(z_0 = \pm 1)$, the difference of which yields the Wigner function value W_ξ . To implement this protocol on a physical level, we have in mind the standard dispersive Hamiltonian for the resonator and the ancilla qubit with frequency $\omega_{\text{Q}}^{(0)}$,

$$\hat{H}_{\text{disp}} = \omega_{\text{R}} \hat{a}^\dagger \hat{a} + \omega_{\text{Q}}^{(0)} |1\rangle\langle 1| - \chi \hat{a}^\dagger \hat{a} |1\rangle\langle 1|. \quad (59)$$

The evolution with \hat{H}_{disp} during time interval δt yields the operator $\hat{U}_\Phi = |0\rangle\langle 0| + e^{i\Phi \hat{a}^\dagger \hat{a}} |1\rangle\langle 1|$ with phase $\Phi = \chi \delta t$. Before the tomography, the ancilla qubit is in the state $|\psi_0\rangle = |0\rangle$; the $X_{\pi/2}$ gate brings it into the superposition $|\psi_1\rangle = \frac{1}{\sqrt{2}}(|0\rangle + i|1\rangle)$. After that, by tuning the

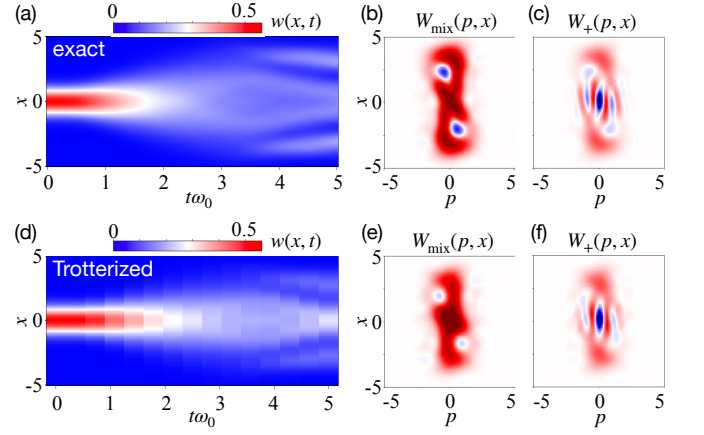


FIG. 9. Numerical simulations of exact and Trotter evolutions. (a) Exact dynamics of the photon probability distribution $w(x, t)$ after the quench during time $t \in [0, t_f]$. Wigner functions at the end of evolution $t = t_f$: (b) W_{mix} without parity selection, and (c) W_+ for the positive parity, which shows cat state signatures. (d-f): The data for $w(x, t)$, W_{mix} , and W_+ emulated by means of our quantum algorithm as depicted in Fig. 8 with $L = 15$ Trotter steps. The parameters are $N = 5$ qubits, a Fock-space cutoff at 20 photons, $\omega_z/\omega_0 = 0.05$, $J/\omega_0 = 1$ and $g/\omega_0 = 0.9$, which places the system slightly above the QPT.

duration δt of the off-resonant evolution such that $\Phi = \pi$, the entangling gate C_π can be realized. Depending on the photon parity, C_π rotates the qubit state either over the angle π or 2π along the Bloch-sphere equator. The ancilla wave function then becomes $|\psi_2\rangle = \frac{1}{\sqrt{2}}(|0\rangle + i\Pi|1\rangle)$. The second $X_{\pi/2}$ gate and subsequent z_0 measurement finalize the Ramsey interferometry. As a result, one measures the state $|\psi_3\rangle = |1\rangle$ if the parity is even ($\Pi = 1$) or $|\psi_3\rangle = |0\rangle$ if the parity is odd ($\Pi = -1$).

V. DISCUSSION

Illustrative results of our numerical simulations of the Dicke-Ising Hamiltonian with $N = 5$ qubits are shown in Fig. 9. Our data include temporal evolution of the photon probability distribution $w(x, t)$ as well as the Wigner functions W_{mix} , W_+ at the very end of the time evolution. In Fig. 9(a) we show the exact dynamics of $w(x, t)$ when the evolution starts with a Gaussian distribution $w(x, 0) = e^{-x^2}/\sqrt{\pi}$, which corresponds the many-body wave function $|\Psi_0\rangle = |\text{FM}\rangle$. At the end of the evolution ($\omega_0 t_f = 5$), the wave function $|\Psi_{t_f}\rangle$ is supposed to be similar to $|\text{SR}\rangle$. The distribution $w(x, t_f)$ indeed has well-defined side peaks around $x \approx \pm 4$, which correspond to a finite amount of condensed photons.

While the Wigner functions W_{mix} and W_+ at $t = t_f$ (Fig. 9(b, c)) look distorted, they are qualitatively similar to the ideal distributions shown in Fig. 1(c, d). It is important to note that W_+ in Fig. 9(c) retains clear cat state signatures, visible as blue stripes of negative quasi-

probabilities. In Fig. 9(d-f), we present the equivalent simulation of the Trotterized dynamics with 15 steps according to our digital-analog algorithm given in Fig. 8. The Wigner functions found through the Trotter evolution (Fig. 9 (e, f)) are in good agreement with the exact simulation results in Fig. 9(b, c), respectively.

For the total gate count, we obtain the following estimation. We do not take into account the gates needed for the Wigner tomography in this estimation and assume the qubit-boson architecture from Fig. 6(a). Each Rabi gate S_R involves three JC gates. The Dicke gate S_D has N S_R -gates and $\frac{1}{2}N(N-1)$ SWAPs. The Dicke-Ising S_{DI} -gate has one S_D -gate and $2(N-1)$ CNOTs. Parity selection involves $(N-1)$ CNOTs. To summarize, the circuit with L Trotter steps requires:

- $\frac{1}{2}LN(N-1)$ SWAPs,
- $(2L+1)(N-1)$ CNOTs,
- $3LN$ JC gates.

Based on these numbers, we conjecture that the algorithm is capable of simulating the QPT after a quench as well as the cat state preparation with a finite depth quantum circuit without fine-tuning parameters.

VI. CONCLUSION AND OUTLOOK

In this work, we proposed a digital-analog quantum algorithm for simulating the superradiant QPT in the Dicke-Ising model, where individual qubits interact with each other and with a common photon mode. The algorithm features a sequence of analog Jaynes-Cummings gates combined with standard digital single-qubit and two-qubit rotations. This quantum circuit is capable of

simulating quench dynamics and the QPT between the normal and superradiant phases. We proposed a protocol based on qubit-parity measurements that allows one to obtain a Schrödinger cat state as the output of resonator Wigner tomography. Additionally, we applied a path-integral description to the model via a bosonic angular representation of the spin operators and formulated the quasi-classical description of fluctuations in the large-spin limit. This approach can be useful for further studies of macroscopic quantum tunneling. Finally, we found that the qubit-qubit interaction leads to an emergent Ising transition driven by the Kibble-Zurek mechanism in imaginary time. The qubit subsystem becomes critical for certain quantum trajectories of the photon field, making the fluctuations in the superradiant phase non-trivial, in contrast to the conventional Dicke model. As an outlook for future investigations in this direction, an interesting question to address is the behavior of the entanglement entropy and the value of the central charge at the QPT and in the superradiant phase.

ACKNOWLEDGMENTS

This work is supported by DPG under Germany's Excellence Strategy – Cluster of Excellence Matter and Light for Quantum Computing (ML4Q) EXC 2004/1 – 390534769. We further acknowledge support from the German Federal Ministry of Education and Research (BMBF) in the funding program "Quantum technologies – from basic research to market", contract numbers 13N15584 (project DAQC) and 13N16149 (project QSolid). We are also grateful to the funding from the Deutsche Forschungsgemeinschaft (DFG, German Research Foundation) - Project-ID 429529648 - TRR 306 QuCoLiMa ("Quantum Cooperativity of Light and Matter"). The authors thank Alessandro Ciani and Alexander Shnirman for their fruitful discussions.

-
- [1] C. F. Lee and N. F. Johnson, First-Order Superradiant Phase Transitions in a Multiqubit Cavity System, *Phys. Rev. Lett.* **93**, 083001 (2004).
 - [2] S. Gammelmark and K. Mølmer, Phase transitions and Heisenberg limited metrology in an Ising chain interacting with a single-mode cavity field, *New Journal of Physics* **13**, 053035 (2011).
 - [3] Y. Zhang, L. Yu, J. Q. Liang, G. Chen, S. Jia, and F. Nori, Quantum phases in circuit QED with a superconducting qubit array, *Scientific Reports* **4**, 4083 (2014).
 - [4] J. Gelhausen, M. Buchhold, A. Rosch, and P. Strack, Quantum-optical magnets with competing short- and long-range interactions: Rydberg-dressed spin lattice in an optical cavity, *SciPost Phys.* **1**, 004 (2016).
 - [5] J. Rohn, M. Hörmann, C. Genes, and K. P. Schmidt, Ising model in a light-induced quantized transverse field, *Phys. Rev. Res.* **2**, 023131 (2020).
 - [6] A. Schellenberger and K. P. Schmidt, (Almost) everything is a Dicke model - Mapping non-superradiant correlated light-matter systems to the exactly solvable Dicke model, *SciPost Phys. Core* **7**, 038 (2024).
 - [7] A. Langheld, M. Hörmann, and K. P. Schmidt, *Quantum phase diagrams of Dicke-Ising models by a wormhole algorithm* (2024), arXiv:2409.15082 [cond-mat.str-el].
 - [8] T. O. Puel and T. Macrì, Confined Meson Excitations in Rydberg-Atom Arrays Coupled to a Cavity Field, *Phys. Rev. Lett.* **133**, 106901 (2024).
 - [9] V. N. Popov and S. Fedotov, The functional integration method and diagram technique for spin systems, *Sov. Phys. JETP* **67**, 535 (1988).
 - [10] C. Emary and T. Brandes, Chaos and the quantum phase transition in the Dicke model, *Physical Review E* **67**, 066203 (2003).
 - [11] P. Eastham and P. Littlewood, Bose condensation of cavity polaritons beyond the linear regime: The thermal

- equilibrium of a model microcavity, *Physical Review B* **64**, 235101 (2001).
- [12] E. G. Dalla Torre, S. Diehl, M. D. Lukin, S. Sachdev, and P. Strack, Keldysh approach for nonequilibrium phase transitions in quantum optics: Beyond the Dicke model in optical cavities, *Physical Review A* **87**, 023831 (2013).
- [13] E. G. Dalla Torre, Y. Shchadilova, E. Y. Wilner, M. D. Lukin, and E. Demler, Dicke phase transition without total spin conservation, *Phys. Rev. A* **94**, 061802 (2016).
- [14] P. Kirton, M. M. Roses, J. Keeling, and E. G. Dalla Torre, Introduction to the Dicke Model: From Equilibrium to Nonequilibrium, and Vice Versa, *Adv. Quantum Technol.* **2**, 1800043 (2019).
- [15] D. S. Shapiro, W. V. Pogosov, and Y. E. Lozovik, Universal fluctuations and squeezing in a generalized Dicke model near the superradiant phase transition, *Phys. Rev. A* **102**, 023703 (2020).
- [16] F. Dimer, B. Estienne, A. S. Parkins, and H. J. Carmichael, Proposed realization of the Dicke-model quantum phase transition in an optical cavity QED system, *Phys. Rev. A* **75**, 013804 (2007).
- [17] P. Nataf and C. Ciuti, Vacuum Degeneracy of a Circuit QED System in the Ultrastrong Coupling Regime, *Phys. Rev. Lett.* **104**, 023601 (2010).
- [18] O. Viehmann, J. von Delft, and F. Marquardt, Superradiant Phase Transitions and the Standard Description of Circuit QED, *Phys. Rev. Lett.* **107**, 113602 (2011).
- [19] K. Baumann, C. Guerlin, F. Brennecke, and T. Esslinger, Dicke quantum phase transition with a superfluid gas in an optical cavity, *Nature* **464**, 1301 (2010).
- [20] X.-F. Zhang, Q. Sun, Y.-C. Wen, W.-M. Liu, S. Eggert, and A.-C. Ji, Rydberg Polaritons in a Cavity: A Superradiant Solid, *Phys. Rev. Lett.* **110**, 090402 (2013).
- [21] M. P. Baden, K. J. Arnold, A. L. Grimsom, S. Parkins, and M. D. Barrett, Realization of the dicke model using cavity-assisted raman transitions, *Phys. Rev. Lett.* **113**, 020408 (2014).
- [22] J. Klinder, H. Kefler, M. Wolke, L. Mathey, and A. Hemmerich, Dynamical phase transition in the open Dicke model, *Proceedings of the National Academy of Sciences* **112**, 3290 (2015), <https://www.pnas.org/doi/pdf/10.1073/pnas.1417132112>.
- [23] A. Safavi-Naini, R. J. Lewis-Swan, J. G. Bohnet, M. Gärttner, K. A. Gilmore, J. E. Jordan, J. Cohn, J. K. Freericks, A. M. Rey, and J. J. Bollinger, Verification of a Many-Ion Simulator of the Dicke Model Through Slow Quenches across a Phase Transition, *Phys. Rev. Lett.* **121**, 040503 (2018).
- [24] J. Klinder, H. Kefler, M. R. Bakhtiari, M. Thorwart, and A. Hemmerich, Observation of a Superradiant Mott Insulator in the Dicke-Hubbard Model, *Phys. Rev. Lett.* **115**, 230403 (2015).
- [25] G. Ferioli, A. Glicenstein, I. Ferrier-Barbut, and A. Browaeys, A non-equilibrium superradiant phase transition in free space, *Nature Physics* **19**, 1345 (2023).
- [26] C. Liedl, F. Tebbenjohanns, C. Bach, S. Pucher, A. Rauschenbeutel, and P. Schneeweiss, Observation of Superradiant Bursts in a Cascaded Quantum System, *Phys. Rev. X* **14**, 011020 (2024).
- [27] J. M. Fink, R. Bianchetti, M. Baur, M. Göppl, L. Steffen, S. Filipp, P. J. Leek, A. Blais, and A. Wallraff, Dressed Collective Qubit States and the Tavis-Cummings Model in Circuit QED, *Phys. Rev. Lett.* **103**, 083601 (2009).
- [28] M. Feng, Y. P. Zhong, T. Liu, L. L. Yan, W. L. Yang, J. Twamley, and H. Wang, Exploring the quantum critical behaviour in a driven Tavis-Cummings circuit, *Nature Communications* **6**, 7111 (2015).
- [29] F. Yoshihara, T. Fuse, S. Ashhab, K. Kakuyanagi, S. Saito, and K. Semba, Superconducting qubit-oscillator circuit beyond the ultrastrong-coupling regime, *Nature Physics* **13**, 44 (2017).
- [30] P. Forn-Díaz, L. Lamata, E. Rico, J. Kono, and E. Solano, Ultrastrong coupling regimes of light-matter interaction, *Rev. Mod. Phys.* **91**, 025005 (2019).
- [31] A. Frisk Kockum, A. Miranowicz, S. De Liberato, S. Savasta, and F. Nori, Ultrastrong coupling between light and matter, *Nature Reviews Physics* **1**, 19 (2019).
- [32] A. Blais, A. L. Grimsom, S. M. Girvin, and A. Wallraff, Circuit quantum electrodynamics, *Rev. Mod. Phys.* **93**, 025005 (2021).
- [33] S. Lloyd, Universal quantum simulators, *Science* **273**, 1073 (1996).
- [34] B. Fauseweh, Quantum many-body simulations on digital quantum computers: State-of-the-art and future challenges, *Nature Communications* **15**, 2123 (2024).
- [35] A. Macridin, P. Spentzouris, J. Amundson, and R. Harnik, Electron-phonon systems on a universal quantum computer, *Phys. Rev. Lett.* **121**, 110504 (2018).
- [36] A. Macridin, P. Spentzouris, J. Amundson, and R. Harnik, Digital quantum computation of fermion-boson interacting systems, *Phys. Rev. A* **98**, 042312 (2018).
- [37] A. Mezzacapo, U. Las Heras, J. S. Pedernales, L. DiCarlo, E. Solano, and L. Lamata, Digital Quantum Rabi and Dicke Models in Superconducting Circuits, *Scientific Reports* **4**, 7482 (2014).
- [38] N. K. Langford, R. Sagastizabal, M. Kounalakis, C. Dickel, A. Bruno, F. Luthi, D. J. Thoen, A. Endo, and L. DiCarlo, Experimentally simulating the dynamics of quantum light and matter at deep-strong coupling, *Nature Communications* **8**, 1715 (2017).
- [39] E. Crane, K. C. Smith, T. Tomesh, A. Eickbusch, J. M. Martyn, S. Kühn, L. Funcke, M. A. DeMarco, I. L. Chuang, N. Wiebe, A. Schuckert, and S. M. Girvin, **Hybrid oscillator-qubit quantum processors: Simulating fermions, bosons, and gauge fields** (2024), [arXiv:2409.03747 \[quant-ph\]](https://arxiv.org/abs/2409.03747).
- [40] G. B. P. Huber, F. A. Roy, L. Koch, I. Tsitsilin, J. Schirck, N. J. Glaser, N. Bruckmoser, C. Schweizer, J. Romeiro, G. Krylov, M. Singh, F. X. Haslbeck, M. Knudsen, A. Marx, F. Pfeiffer, C. Schneider, F. Wallner, D. Bunch, L. Richard, L. Södergren, K. Liegener, M. Werninghaus, and S. Filipp, **Parametric multi-element coupling architecture for coherent and dissipative control of superconducting qubits** (2024), [arXiv:2403.02203 \[quant-ph\]](https://arxiv.org/abs/2403.02203).
- [41] Z. Leghtas, G. Kirchmair, B. Vlastakis, M. H. Devoret, R. J. Schoelkopf, and M. Mirrahimi, Deterministic protocol for mapping a qubit to coherent state superpositions in a cavity, *Phys. Rev. A* **87**, 042315 (2013).
- [42] B. Vlastakis, G. Kirchmair, Z. Leghtas, S. E. Nigg, L. Frunzio, S. M. Girvin, M. Mirrahimi, M. H. Devoret, and R. J. Schoelkopf, Deterministically Encoding Quantum Information Using 100-Photon Schrödinger Cat States, *Science* **342**, 607 (2013).
- [43] A. Grimm, N. E. Frattini, S. Puri, S. O. Mundhada, S. Touzard, M. Mirrahimi, S. M. Girvin, S. Shankar, and M. H. Devoret, Stabilization and operation of a Kerr-cat

- qubit, *Nature* **584**, 205 (2020).
- [44] R. Lescanne, M. Villiers, T. Peronin, A. Sarlette, M. Delbecq, B. Huard, T. Kontos, M. Mirrahimi, and Z. Leghtas, Exponential suppression of bit-flips in a qubit encoded in an oscillator, *Nature Physics* **16**, 509 (2020).
- [45] Y. Xu, D. Fallas Padilla, and H. Pu, Multicriticality and quantum fluctuation in a generalized Dicke model, *Phys. Rev. A* **104**, 043708 (2021).
- [46] Y. Salathé, M. Mondal, M. Oppliger, J. Heinsoo, P. Kurpiers, A. Potočnik, A. Mezzacapo, U. Las Heras, L. Lamata, E. Solano, S. Filipp, and A. Wallraff, Digital Quantum Simulation of Spin Models with Circuit Quantum Electrodynamics, *Phys. Rev. X* **5**, 021027 (2015).
- [47] D. Wecker, M. B. Hastings, N. Wiebe, B. K. Clark, C. Nayak, and M. Troyer, Solving strongly correlated electron models on a quantum computer, *Phys. Rev. A* **92**, 062318 (2015).
- [48] L. G. Lutterbach and L. Davidovich, Method for Direct Measurement of the Wigner Function in Cavity QED and Ion Traps, *Phys. Rev. Lett.* **78**, 2547 (1997).

Appendix A: Mean-field free energy for Dicke-Ising Hamiltonian at $\omega_z = 0$

In this part of the Appendix, we derive the free energy (20) from the Hamiltonian (1) assuming $\omega_z = 0$. In the limit of zero ω_z , only two types of spin operators remain in the Hamiltonian, σ_q^x and $\sigma_q^z \sigma_{q+1}^z$. Applying the Jordan-Wigner representation to them gives

$$\hat{\sigma}_q^x = \hat{c}_q^\dagger \hat{c}_q - \hat{c}_q \hat{c}_q^\dagger, \quad \hat{\sigma}_q^z \hat{\sigma}_{q+1}^z = \hat{c}_q^\dagger \hat{c}_{q+1} + \hat{c}_{q+1}^\dagger \hat{c}_q + \hat{c}_q^\dagger \hat{c}_{q+1}^\dagger + \hat{c}_{q+1} \hat{c}_q. \quad (\text{A1})$$

The Hamiltonian (1) after this transformation has bilinear fermion combinations,

$$\hat{H}_{\text{DI}} = \omega_0 \hat{a}^\dagger \hat{a} - J \sum_{q=1}^N (\hat{c}_q^\dagger \hat{c}_{q+1} + \hat{c}_{q+1}^\dagger \hat{c}_q + \hat{c}_q^\dagger \hat{c}_{q+1}^\dagger + \hat{c}_{q+1} \hat{c}_q) + \frac{g}{\sqrt{N}} (\hat{a}^\dagger + \hat{a}) \sum_{q=1}^N (\hat{c}_q^\dagger \hat{c}_q - \hat{c}_q \hat{c}_q^\dagger). \quad (\text{A2})$$

We note that for $\omega_z \neq 0$ additional terms $\sim \hat{\sigma}_q^z$ arise, yielding nonlocal fermion strings and resulting in a more complicated derivation of the free energy. Consider the partition function $Z = \text{tr}(e^{-\hat{H}_{\text{DI}}/T})$ at finite temperature T . It is reduced to the Matsubara path integral

$$Z = \int d[a, \bar{a}, c, \bar{c}] e^{-S[a, \bar{a}, c, \bar{c}]} \quad (\text{A3})$$

over complex boson fields $a(\tau), \bar{a}(\tau)$ and Grassmann fields $c_q(\tau), \bar{c}_q(\tau)$, where τ is the imaginary time $\tau \in [0, 1/T]$. These fields describe, respectively, photons and Jordan-Wigner fermions. The Matsubara action in (A3) is

$$S = \int_0^{1/T} d\tau \left(\bar{a} \partial_\tau a + \sum_{q=1}^N \bar{c}_q \partial_\tau c_q + H_{\text{DI}}[a, \bar{a}, c, \bar{c}] \right). \quad (\text{A4})$$

Assuming periodic boundary conditions for the Ising chain, we introduce the wave numbers $\mathbf{k} = \frac{2\pi n}{N} - \pi$ with $0 \leq n < N$ spanning a Brillouin zone. The Fourier transformation into \mathbf{k} -space for Grassmann fields reads $c_{\mathbf{k}} = \frac{1}{\sqrt{N}} \sum_{q=1}^N e^{-i\mathbf{k}q} c_q$. The action (A4) can be parametrized via Nambu vectors $\Psi_{\mathbf{k}} = [c_{\mathbf{k}} \quad \bar{c}_{-\mathbf{k}}]^T$ in γ -space resulting in the following form:

$$S = S_{\text{ph}} - \frac{1}{2} \sum_{\mathbf{k}} \int_0^{1/T} d\tau \Psi_{-\mathbf{k}}^T \gamma_x G_{\mathbf{k}}^{-1} [a, \bar{a}] \Psi_{\mathbf{k}}, \quad (\text{A5})$$

where the inverted Green function (Lagrangian) reads

$$-G_{\mathbf{k}}^{-1} [a(\tau), \bar{a}(\tau)] = \begin{bmatrix} \partial_\tau - 2J \cos \mathbf{k} + 2g(\bar{a}(\tau) + a(\tau))/\sqrt{N} & -2iJ \sin \mathbf{k} \\ 2iJ \sin \mathbf{k} & \partial_\tau + 2J \cos \mathbf{k} - 2g(\bar{a}(\tau) + a(\tau))/\sqrt{N} \end{bmatrix} \quad (\text{A6})$$

and

$$S_{\text{ph}} = \int_0^{1/T} d\tau (\bar{a} \partial_\tau a + \omega_0 \bar{a} a) \quad (\text{A7})$$

is the free photon action. Note, that $G_{\mathbf{k}}^{-1}[a, \bar{a}]$ is a nonstationary matrix because of time-dependent a -fields and, therefore, an inversion is a nontrivial task. Below we tackle this problem in a mean-field approximation.

We parametrize the complex \bar{a} and a through real fields u and v ,

$$a(\tau) = \sqrt{N} \frac{u(\tau) + iv(\tau)}{2}, \quad \bar{a}(\tau) = \sqrt{N} \frac{u(\tau) - iv(\tau)}{2}. \quad (\text{A8})$$

After a Fourier transformation defined as $a(\tau) = \sum_n a_n e^{-i2\pi n T \tau}$ and $\bar{a}(\tau) = \sum_n a_n e^{i2\pi n T \tau}$, we take the Gaussian integrals over real boson v_n and real Grassmann $\Psi_{\mathbf{k}}$ fields. As a result, we receive an effective action for the real boson $u(\tau)$, which is a sum of the free boson action S_u and the spin contribution given by the logarithm of the fermion determinant,

$$S_{\text{eff}} = \frac{1}{4} N \int_0^{1/T} \left(\frac{1}{\omega_0} (\partial_\tau u)^2 + \omega_0 u^2 \right) d\tau - \frac{1}{2} \ln \det(-G_{\mathbf{k}}^{-1}[u]). \quad (\text{A9})$$

It features the inverted Green function (A6) written as $G_{\mathbf{k}}^{-1}[u] = -\gamma_0 \partial_\tau - H_{\mathbf{k}}(\tau)$, where the τ -dependent Hamiltonian matrix in Nambu γ -space reads

$$H_{\mathbf{k}}(\tau) = -2J(\gamma_z \cos \mathbf{k} - \gamma_y \sin \mathbf{k}) + 2g\gamma_z u(\tau). \quad (\text{A10})$$

In the mean-field approximation, we assume $u(\tau) = \text{const}$ neglecting temporal fluctuations. The fermion determinant in (A9) can be found analytically through an infinite product over Matsubara frequencies with 2×2 γ -matrix determinants,

$$\ln \det(G_{\mathbf{k}}^{-1}[u] G_{\mathbf{k}}[0]) = N \int_{-\pi}^{\pi} \frac{d\mathbf{k}}{2\pi} \ln \left(\prod_n \frac{\det_\gamma(-i2\pi n T \gamma_0 - 2J(\gamma_z \cos \mathbf{k} - \gamma_y \sin \mathbf{k}) + 2g\gamma_z u)}{\det_\gamma(-i2\pi n T \gamma_0 - 2J(\gamma_z \cos \mathbf{k} - \gamma_y \sin \mathbf{k}))} \right). \quad (\text{A11})$$

We added $G_{\mathbf{k}}[0]$ to regularize the action. This factor emerges from normalizing the partition sum by its value at $g = 0$. To compute the infinite product we use the identity

$$\prod_{n \geq 1} (1 + x^2/n^2) = \frac{1}{\pi \sqrt{x}} \sinh(\pi|x|). \quad (\text{A12})$$

Taking the leading term $\sim \frac{1}{T}$ in the limit of low temperatures, and then integrating over \mathbf{k} , we arrive at the mean-field action

$$S_{\text{mf}} = N \int_0^{1/T} \left(\frac{(\partial_\tau u)^2}{4\omega_0} + \mathcal{F}(u) \right) d\tau \quad (\text{A13})$$

with the normalized free energy $\mathcal{F}(u) = \frac{1}{N} F_{\text{DI}}(u)$ provided in Eq. (21),

$$\mathcal{F}(u) = \frac{1}{4} \omega_0 u^2 - \frac{2}{\pi} (J + g|u|) \text{E} \left[\frac{4gJ|u|}{(J + g|u|)^2} \right]. \quad (\text{A14})$$

Appendix B: Instanton trajectory

Consider the mean-field part of the action (A13). When the system is in the superradiant phase, a variation of S_{mf} by u yields the equation for an instanton saddle-point trajectory,

$$\partial_\tau^2 u - 2\omega_0 \partial_u \mathcal{F}(u) = 0, \quad (\text{B1})$$

with boundary conditions $u(\tau = 0) = -u(\tau = 1/T) = -u_0$, where $u_0 > 0$ is a nonzero solution of the equation $\partial_u \mathcal{F}(u) = 0$ for the superradiant order parameter. There is also an integral motion, which is analogous to the full energy in classical mechanics. It reads

$$-\frac{(\partial_\tau u)^2}{4\omega_0} + \mathcal{F}(u) = \mathcal{F}(-u_0) \quad (\text{B2})$$

where the constant $\mathcal{F}(-u_0)$ is given by the free energy minimum at $u = -u_0$. The instanton solution is given by an *implicit* function $u_{\text{inst}}(\tau)$, which follows from Eq. (B2) as

$$\tau = \int_{-u_0}^{u_{\text{inst}}(\tau)} \frac{du}{\sqrt{2\omega_0(\mathcal{F}(u) - \mathcal{F}(-u_0))}}. \quad (\text{B3})$$

The schematic shape of the solution that follows from this integral is presented in Fig. 3(c).